Ground-Motion Variability for Ruptures on Rough Faults

Jagdish Chandra Vyas*[1], Martin Galis[2,3], and P. Martin Mai[1]

ABSTRACT

Fault roughness influences earthquake rupture dynamics, seismic energy radiation, and, hence, resulting ground motion and its variability. Using 3D dynamic rupture simulations considering a range of rough-fault realizations, we investigate the effects of rupture complexity caused by fault roughness on ground-motion variability, that is, the variability of peak ground acceleration (PGA) and velocity (PGV) as a function of distance. In our analysis, we vary hypocenter locations (leading to unilateral and bilateral ruptures) and fault roughness amplitude to generate a set of magnitude $M \approx 7$ strike-slip dynamic rupture simulations. Synthetic seismic waveforms computed on a dense set of surface sites (maximum resolved frequency 5.75 Hz) form our database for detailed statistical analyses. For unilateral ruptures, our simulations reveal that ground-shaking variability (in terms of PGA and PGV) remains nearly constant with increasing distance from the fault. In contrast, bilateral ruptures lead to slowly decreasing ground-motion variability with increasing distance in the near field (less than 20 km). The variability becomes almost constant at large fault distances. We also find that low-amplitude fault roughness leads to ruptures that are likely to generate higher PGA variability than events on faults with high-amplitude roughness. Increasing fault roughness distorts the radiation pattern, thereby reducing directivity effects and, hence, potentially lowering ground-motion variability. The average PGV variability from our rough-fault rupture models is consistent with estimates from empirical ground-motion models (GMMs). However, the average PGA variability exceeds the variability encoded in empirical GMMs by nearly 20%. Hence, our findings have implications for near-source ground-motion prediction in seismic hazard studies, because ground-motion variability depends on details of the earthquake rupture process and is larger than GMM estimates.

KEY POINTS

- We investigate how fault roughness impacts earthquake ground-motion variability.
- Peak ground velocity variability aligns with empirical models; peak ground acceleration variability exceeds estimates by nearly 20%.
- The ground-motion variability depends on rupture details, challenging seismic hazard estimation.

Supplemental Material

INTRODUCTION

To estimate the potential shaking during future earthquakes, seismic hazard analysis involves primarily empirical ground-motion models (GMMs) that are based on recorded datasets from past earthquakes. Empirical GMMs estimate the natural logarithm of the median and standard deviation of ground-motion parameters, such as peak ground velocity (PGV), peak ground acceleration (PGA), and pseudospectral acceleration (Abrahamson and Silva, 2008; Boore and Atkinson, 2008; Campbell and Bozorgnia, 2008, 2014; Chiou and Youngs, 2008, 2014; Abrahamson *et al.*, 2014; Boore *et al.*, 2014). The standard deviation, also referred to as ground-motion variability, is a fundamental parameter for probabilistic seismic hazard analysis (PSHA). It controls the shape of the resulting hazard curves, especially at long return periods and low probabilities of exceedance (Bommer and Abrahamson, 2006). Hence, it is necessary to understand the physical processes governing ground-motion variability to obtain more reliable estimates from PSHA.

1. King Abdullah University of Science and Technology (KAUST), Jeddah, Saudi Arabia, https://orcid.org/0000-0001-7199-1460 (JCV); https://orcid.org/0000-0002-9744-4964 (PMM); 2. Department of Astronomy, Physics of the Earth, and Meteorology, Faculty of Mathematics, Physics and Informatics, Comenius University, Bratislava, Slovakia; 3. Earth Science Institute, Slovak Academy of Sciences, Slovak Academy of Sciences, Bratislava, Slovakia

*Corresponding author: jagdish.vyas@kaust.edu.sa

Cite this article as Vyas, J. C., M. Galis, and P. M. Mai (2023). Ground-Motion Variability for Ruptures on Rough Faults, *Bull. Seismol. Soc. Am.* **114**, 965–981, doi: 10.1785/0120230117

The investigation of the physical processes governing high-frequency ground motion and its variability remains an ongoing endeavor. According to dynamic rupture simulations (e.g., Dunham *et al.*, 2011; Shi and Day, 2013; Mai *et al.*, 2018; Taufiqurrahman *et al.*, 2022), fault roughness contributes to the emission of high frequencies through the acceleration and deceleration of the rupture front. In addition, observed ground-motion spectra suggest a high-frequency roll-off beyond a specific maximum frequency, denoted as $f_{\max}$ (Hanks, 1982). Another approach to model the decay of such high frequencies involves the use of a high-cut κ-filter (Anderson and Hough, 1984). The underlying physical causes of this high-frequency roll-off and filtering are still the subject of research. For example, Papageorgiou and Aki (1983a,b) attribute it to nonelastic material behavior at the rupture tip (source effects), whereas others, like Hanks (1982) and Anderson and Hough (1984), consider it to be related to local site conditions (site effects). Recently, Beresnev (2019) provided an interpretation that considers $f_{\max}$ and κ as source effects by relating earthquake source spectra to ω^n law with a noninteger n. This interpretation indicates that $\omega^{2.5}$ offers a spectral falloff consistent with using $f_{\max}$ or κ filters, suggesting that high-cut filtering is naturally associated with source effects. In this study, the scale of fault roughness determines the maximum frequency radiated off the fault, implying that it is entirely a source effect. This source effect significantly influences ground-motion behavior and its variability.

Ground-motion variability is typically divided into epistemic uncertainty and aleatory variability. Epistemic uncertainty describes scientific uncertainty due to incomplete data, a lack of knowledge, and imperfect modeling. Therefore, given a deeper understanding of physical processes, increased datasets, and improved modeling and simulation techniques, the epistemic uncertainty theoretically should be reducible and eventually approach zero (Atik *et al.*, 2010). In contrast, aleatory variability is related to the natural randomness of physical processes and, therefore, cannot be reduced as such.

Earlier studies separate and quantify components of aleatory variability and epistemic uncertainty (Anderson and Brune, 1999; Atkinson, 2013), whereby the variability can be further subdivided into within-event (intraevent) and between-event (interevent) components (Strasser *et al.*, 2009; Atik *et al.*, 2010). The within-event component is estimated by considering all ground-motion records at a particular source-to-site distance from a single event, whereas the between-event component is calculated by considering records at a given site from all the events. In this study, we examine within-event ground-motion variability due to earthquake source processes only, focusing on the effects of rupture complexity on high-frequency ground motions due to the intricate dynamics in the presence of fault roughness. We consider strike-slip earthquakes in a narrow magnitude range, occurring on an overall vertical fault.

Previously, empirical GMMs were formulated assuming uniform ground-motion variability (e.g., Boore *et al.*, 1997; Atkinson and Boore, 2006; Chiou and Youngs, 2006; Boore and Atkinson, 2008); however, more recent empirical GMMs considered variability to depend on earthquake magnitude and source-to-site distance (e.g., Abrahamson and Silva, 2008; Chiou and Youngs, 2008, 2014; Abrahamson *et al.*, 2014; Boore *et al.*, 2014). More refined estimates of ground-motion variability suffered from the lack of ground-motion recordings, particularly at near-fault distances (R_{JB} < 10–20 km) for larger magnitudes (M > 7) (Strasser *et al.*, 2009; Paolucci *et al.*, 2014). To overcome this data gap, physics-based ground-motion modeling techniques are considered that account for complex rupture processes and 3D wave propagation effects (Spudich and Frazer, 1984; Komatitsch and Tromp, 1999; Hartzell *et al.*, 2005; Dumbser and Käser, 2006; Moczo *et al.*, 2007; Galis *et al.*, 2008; Graves and Pitarka, 2010; Mai *et al.*, 2010, 2018) that augment the database of recorded ground motions.

Kinematic ground-motion computations have been most widely used in the past, but dynamic rupture simulations have became more common recently. Kinematic ground-motion simulations specify the spatiotemporal evolution of the rupture process ad hoc in advance. Being conceptually simple, the computational demands depend on the chosen earthquake source characterization and Earth structure model. Such simulations have been used to better understand general aspects of ground-motion variability in the context of variations in the rupture process and 3D Earth structure (Beauval *et al.*, 2009; Mena and Mai, 2011; Imperatori and Mai, 2012; Imtiaz *et al.*, 2015; Ramirez-Guzman *et al.*, 2015; Douglas and Aochi, 2016; Graves and Pitarka, 2016; Vyas *et al.*, 2016; Gallovič, 2017; Iwaki *et al.*, 2017; Crempien and Archuleta, 2018; Frankel *et al.*, 2018; Sun *et al.*, 2018). Imtiaz *et al.* (2015) analyzed waveforms computed from various vertical strike-slip kinematic rupture models. They found that the within-event variability decreases with increasing distance for unilateral ruptures but increases for bilateral ruptures. Vyas *et al.* (2016) used rupture models of the 1992 M_{w} 7.3 Landers earthquake and the M_{w} 7.8 ShakeOut scenario to investigate the within-event variability. They found that variability depends on source-to-site distance and azimuth, and decreases with increasing distance following a power law (whereby the power law decay appears to be controlled by slip heterogeneity). Gallovič (2017) analyzed ground-motion variability by modeling scenarios of the 2014 M_{w} 6.0 South Napa earthquake. They proposed a model that captures azimuthal variations of between-event variability to refine empirical GMMs. Crempien and Archuleta (2018) used kinematic rupture scenarios on a vertical strike-slip fault to analyze ground-motion variability. They discovered that both the between-event and within-event variabilities increase with increasing correlation length of on-fault slip, whereby the within-event variability is consistently higher than the between-event variability for all correlation lengths.

In contrast, in dynamic rupture simulations, the space-time rupture evolution follows a physically self-consistent process based on assumed fault-frictional conditions, the applied initial stress, the fault-plane geometry, and 3D Earth structure. Besides studying fundamental earthquake source physics, dynamic rupture simulations have been used to investigate ground-motion behavior and its variability (Guatteri *et al.*, 2003; Harris, 2004; Aochi and Douglas, 2006; Ripperger *et al.*, 2008; Shi and Day, 2013; Baumann and Dalguer, 2014; Harris *et al.*, 2018; Bydlon *et al.*, 2019; Withers, Olsen, Day, *et al.*, 2019, Withers, Olsen, Shi, *et al.*, 2019; Valentová *et al.*, 2021). Ripperger *et al.* (2008) analyzed ground-motion variability from dynamic rupture simulations by considering heterogeneous initial on-fault shear stress. They found that the contribution from stress heterogeneity to the overall ground-motion variability is the strongest for sites close to the fault and experiencing backward directivity for unilateral ruptures. Their study also shows that the hypocenter-station configuration more strongly affects between-event variability than rupture complexity due to stress heterogeneities. Withers, Olsen, Day, *et al.* (2019) performed dynamic rupture simulations that account for fault roughness and 3D Earth structure, including small-scale structural heterogeneities. Their simulations suggest that these small-scale heterogeneities have a strong impact on ground-motion behavior and variability. Recently, Valentová *et al.* (2021) analyzed ground-motion variability from almost 3000 dynamic rupture scenarios on a vertical strike-slip fault. They found that the within-event variability is lower than estimated in empirical GMMs, and reported that the within-event variability from their simulations is larger at stations close to the fault and weakly depends on the spectral response period.

Although the previous studies have investigated ground-motion variability as a function of parameters used in GMMs (e.g., source-to-site distance, azimuth, earthquake magnitude, and spectral response period) using both kinematic and dynamic rupture simulations, several aspects of the source-related ground-motion variability remain elusive. Therefore, we aim to gain a deeper understanding of the within-event variability at high frequencies (up to ~6 Hz) through dynamic rupture simulations accounting for fault roughness. For this purpose, we examine the previous earthquake ground-motion simulations from dynamic rupture models by Mai *et al.* (2018). Although their study focused on the intricacies of the dynamic rupture process due to fault roughness, here we analyze ground-motion variability. We examine the effects of earthquake rupture complexity due to fault roughness on within-event variability as a function of distance. Accordingly, we vary fault roughness amplitude and hypocenter locations (causing unilateral and bilateral ruptures). Our goal is to understand the physics and parameter dependencies of ground-motion variability. Our results, although not providing corrections to empirical GMMs, may eventually be useful for the future developments of GMMs.

TABLE 1
Modeling Parameters and Physical Characteristics

	Variable	Notation	Value
Material properties			
	P-wave velocity	V_P	6 km/s
	S-wave velocity	V_S	3.464 km/s
	Density	ρ	2700 kg/m^3
Frictional properties			
	Static friction coefficient	μ_s	0.677
	Dynamic friction coefficient	μ_d	0.373
	Slip-weakening distance	d_c	0.4 m

OVERVIEW OF RUPTURE MODELS AND COMPUTATIONAL MODEL

Let us briefly review the simulation approach of Mai *et al.* (2018), summarizing their rough-fault parameterizations and computational model. Mai *et al.* (2018) solve the dynamic rupture process on a vertical but fractally rough strike-slip fault governed by a linear slip-weakening friction law. They parameterize fault roughness as geometrical off-fault deviations from a perfectly planar fault reaching the surface (with dimensions 30 km × 15 km), with random realizations that obey the power spectral density $P(k)$ of the von Karman autocorrelation function:

$$P(k) = \frac{4\pi a^2 S^2 H}{(1 + k^2 a^2)^{H+1}}, \quad (1)$$

in which k is wave number, S standard deviation, a correlation length, and H Hurst exponent. Using the approach of Pardo-Iguzquiza and Chica-Olmo (1993), a 2D random field, $f(x,y)$, with a zero mean and unit standard deviation is generated. The off-fault geometrical deviations from a planar surface are then

$$z_{\mathrm{FR}}(x,y) = \alpha \times L \times f(x,y), \quad (2)$$

in which L is the fault length, and α quantifies the amplitude of the roughness. They considered correlation length 3 km, Hurst exponent $H = 1$ (consistent with the assumption of self-similar fractal surfaces), and two levels of roughness amplitude: $\alpha = 0.005$ and $\alpha = 0.0075$. They considered constant regional tectonic stress, but the shear and normal stresses along the fault are heterogeneous due to the nonplanar geometry of the fault. The fault has uniform frictional properties and is embedded in a homogeneous medium without considering intrinsic attenuation (see Table 1).

The simulations are conducted to achieve nucleation and sustained rupture propagation in two steps. First, the resulting fault roughness is periodically shifted so that a region, which is naturally the closest to failure is located at the desired hypocenter location. Then, the shear traction inside the circular

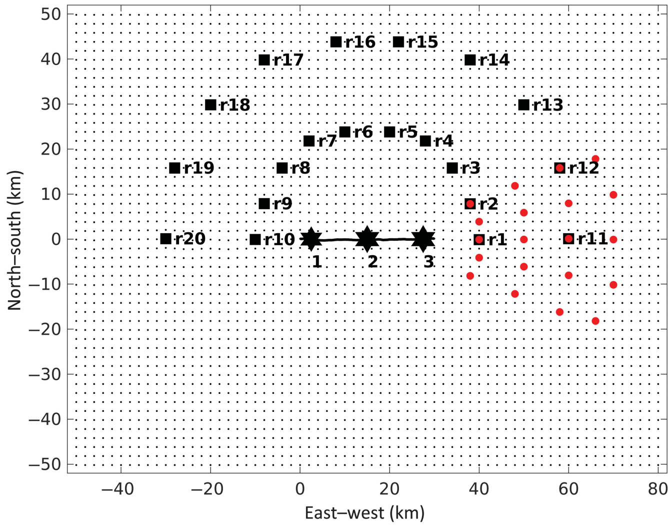

Figure 1. Distribution of receivers at the Earth surface at which we stored simulated ground motions. Black dots mark receivers in the dense grid (spacing 2 km × 2 km) used in the statistical analysis. The squares (r1–r20) indicate selected receivers used for analyzing ground acceleration waveforms, peak ground acceleration (PGA), and peak ground velocity residuals. Red circles mark receiver locations used to assess the Fourier amplitude spectrum (FAS) ratio between fault-normal (FN) and fault-parallel (FP) acceleration waveforms. The black line depicts the fault surface trace, and the black stars indicate the three considered epicenter locations.

nucleation patch is increased, following Galis *et al.* (2015). The numerical parameters are defined to compute the seismic wave field to the maximum resolved frequency $f_{\max} \approx 5.75$ Hz, using a generalized finite-difference method (Ely *et al.*, 2008, 2009). The resulting ground motions are stored on a dense grid of 3366 virtual receivers at the free surface (Fig. 1), covering Joyner–Boore distances (R_{JB}) up to 50 km. Using this database of simulated three-component seismograms enables us to conduct a statistically robust analysis of how rupture style and fault roughness affect ground-motion variability.

For our analysis, we use ground motions for the eighteen dynamic rupture models by Mai *et al.* (2018) that span the magnitude range $6.82 \le M \le 6.95$ (see Table 2). We consider models with three different realizations of fault roughness, two different values of height of fault roughness, α, and three hypocenter locations. Model names consist of a capital letter denoting the combination of realization and α, and a number indicating the hypocenter location. For example, models A1–A3 share the same roughness realization ($\alpha = 0.005$, identical random-seed number), but they have different hypocenter locations. Consequently, A1 produces a rupture propagating to the right, A2 produces a bilateral rupture, and A3 produces a rupture propagating to the left (see Fig. 2). Models A and B share the same spatial distribution of fault roughness (identical seed number), but models A are smoother ($\alpha = 0.005$) than models B ($\alpha = 0.0075$). Similarly, models D and F are rougher versions of models C and E, respectively. Using models A1, C1, and E1,

TABLE 2
Parameters for the 18 Rough-Fault Rupture Models from Mai *et al.* (2018)

Model Name	Realization (Seed Number)	Fault Roughness (RMS/L)	Hypocenter Location	M_w
A1	87	0.005	Left	6.87
A2	87	0.005	Center	6.89
A3	87	0.005	Right	6.87
B1	87	0.0075	Left	6.83
B2	87	0.0075	Center	6.85
B3	87	0.0075	Right	6.83
C1	29	0.005	Left	6.87
C2	29	0.005	Center	6.9
C3	29	0.005	Right	6.87
D1i	29	0.0075	Left	6.84
D2	29	0.0075	Center	6.87
D3i	29	0.0075	Right	6.84
E1	404	0.005	Left	6.88
E2	404	0.005	Center	6.89
E3i	404	0.005	Right	6.95
F1	404	0.0075	Left	6.82
F2	404	0.0075	Center	6.82
F3i	404	0.0075	Right	6.87

the three fault roughness realizations are compared in Figure S1, available in the supplemental material to this article.

Let us observe that adding the fault roughness results in complex dynamic rupture propagation with multiple propagating rupture fronts. This complexity is also reflected in the shape of slip velocity functions, which exhibit diverse durations and complex shapes with multiple peaks along the entire fault, as discussed in more detail in Mai *et al.* (2018).

SIMULATED WAVEFORMS, PGAs, AND OVERALL CONSISTENCY WITH GMMs

In this section, we analyze simulated waveforms, wavefield snapshots, and the spatial distribution of PGA to qualitatively understand the effects of rupture complexity on ground-motion behavior. Because Mai *et al.* (2018) focused on the intricacies of the dynamic rupture process due to fault roughness, they did not compare ground motions with empirical GMMs. Therefore, we also demonstrate the overall consistency of PGA and PGV values from the simulations with empirical GMM-based estimates.

Synthetic waveforms and wavefield snapshots

Let us first examine how fault roughness and hypocenter location affect seismic waveforms and related ground-motion patterns. Figure 3 compares ground acceleration at two stations (r3, r13) for four selected dynamic rupture models (A1, A2, B1, B2). Recall that models A1 and A2 (similarly, models B1 and B2) have different hypocenter locations for the given roughness realization and α, whereas models A1 and B1

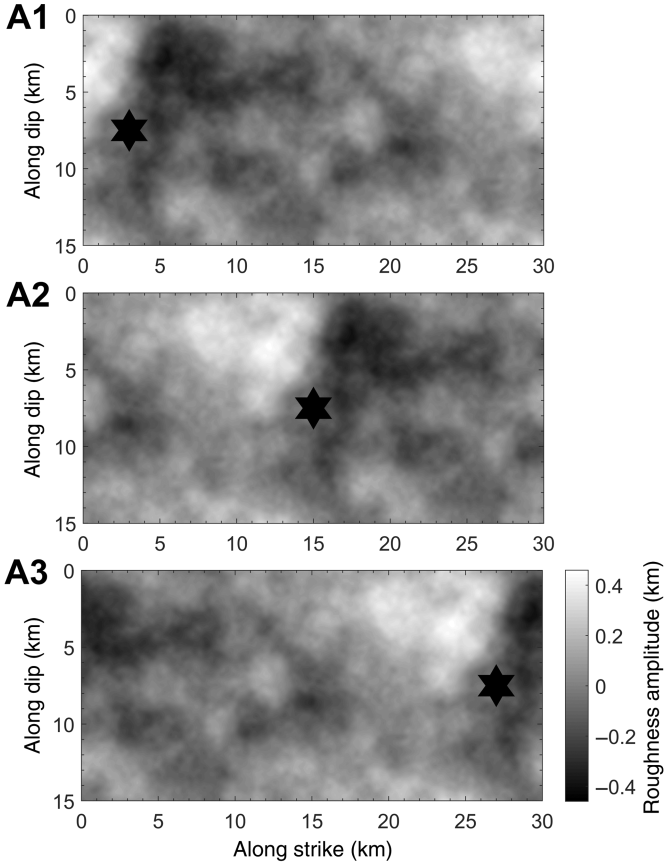

Figure 2. Amplitude variations of fault roughness as off-fault deviations from a planar surface for rupture models A1–A3. The relative position of the hypocenter (indicated by the black star) and fault roughness remain the same. Because of the varying relative positions of the hypocenter and the fault surface, the models produce ruptures propagating toward the right, bilaterally, and left, respectively.

(likewise, models A2 and B2) have different α but the same realization and hypocenter location. We observe differences in arrival times, duration of shaking, and the maximum amplitudes of ground acceleration. For example, later first arrivals in model A1, compared to B1, at station r3 are due to a complex rupture process that results in an overall lower rupture speed. Furthermore, intricate rupture due to fault roughness generates "coda wave" signatures; for example, see waveforms from model B2 at station r3. Differences only in roughness amplitude significantly influence maximum acceleration amplitudes over parts of the receiver grid, thereby affecting ground-motion variability. For example, the maximum acceleration amplitudes at station r13 for the NS component are nearly 1.3 times larger for source model B1 than for A1, whereas 1.8 times larger for model B2 than A2. Differences only in hypocenter location between models A1 (unilateral rupture) and A2 (bilateral rupture) generate ~1.7 times smaller maximum acceleration amplitudes for A2 than for A1 (and ~1.3 times smaller for model B2 than for B1). Similar effects on strong variations in waveform characteristics can also be seen for velocity time series but less pronounced compared to acceleration time series (compare Fig. 3 with Fig. S2). Therefore, the rupture style due to hypocenter locations and fault roughness amplitude significantly affect ground-motion behavior. This motivates us to analyze related shaking variability using acceleration and velocity waveforms stored on a dense receiver grid.

Next, we analyze fault roughness effects on the overall seismic wavefield. As an example, Figure 4 displays snapshots of ground acceleration for rupture model A1. To first order, circular *P* and *S* waves can be observed, which are followed by pronounced "coda waves." These "coda waves" are not due to seismic scattering in a heterogeneous medium. Instead, they are an effect of the rough-fault dynamic rupture process, comprising space-time variations of the rupture speed (leading to radiation of high-frequency seismic waves at "unpredictable or random" times during the rupture propagation) and spatial variations of slip direction (leading to "random" orientation of radiation from individual fault patches). The resulting incoherent radiation causes a complex seismic wavefield even at near-fault distances, which is smoothed as the waves travel away from the fault due to wavefront healing and geometrical spreading. Correspondingly, one can expect large ground-motion variability, in particular in the near-field region. Similar effects can be seen on snapshots of ground velocity (compare Fig. 4 with Fig. S3).

Qualitative analysis of spatial distribution of PGA and PGV

We compute PGA and PGV by rotating the two orthogonal horizontal components (east–west and north–south) from 1° to 90° in steps of 1° and calculating the geometric mean for each pair; the resulting GMRotD50 then represents the sensor-orientation-independent PGA (or PGV) value (Boore *et al.*, 2006). We first analyze spatial variations of PGA, then compare simulated PGA against empirical GMMs and examine PGA residuals at a few stations.

First, we examine PGA maps to qualitatively understand the effects of rupture complexity on ground-motion patterns. Figure 5 compares the spatial distributions of PGA for four selected dynamic rupture models (A1, A2, B1, and B2). Figure S4 shows similar PGA maps for all the eighteen considered rupture models of Mai *et al.* (2018). For rupture models A1 and B1, we observe strong directivity, causing high PGA values in the forward rupture propagation direction (Fig. 5). Directivity effects are more pronounced at near-fault distances, which suggest higher ground-motion variability at such short site-to-rupture distances. However, the spatial distributions of PGA values are more complicated for bilateral ruptures, with models A2 and B2 having higher PGAs toward both the ends of the fault. Therefore, we expect different properties for the near-fault ground-motion variability when comparing unilateral with bilateral ruptures. The spatial distributions of PGV show similar features as PGA distributions, such as higher PGVs in the

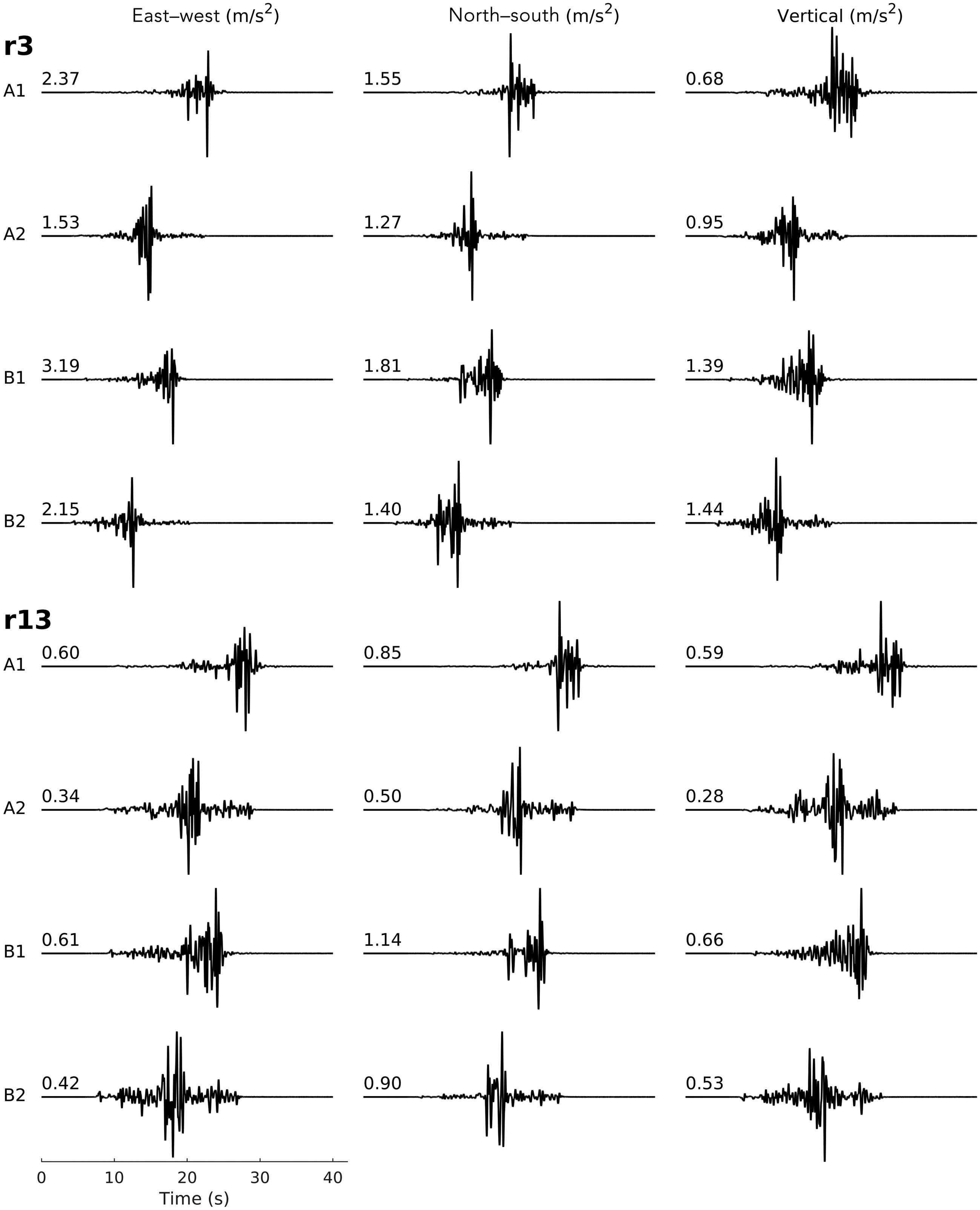

Figure 3. East–west, north–south, and vertical components of ground acceleration for four selected rough-fault models (A1, A2, B1, B2) at two stations (r3 and r13, see Fig. 1). Waveforms are normalized to the absolute maximum of each trace (indicated in the upper left corner).

forward rupture direction for unilateral ruptures and a more complex pattern for bilateral ruptures (compare Figs. S5 and S4).

Next, we compare simulated PGAs from all receivers and all rupture models with PGA estimates of an empirical GMM (Boore *et al.*, 2014; BEA14). Our simulated wavefield is

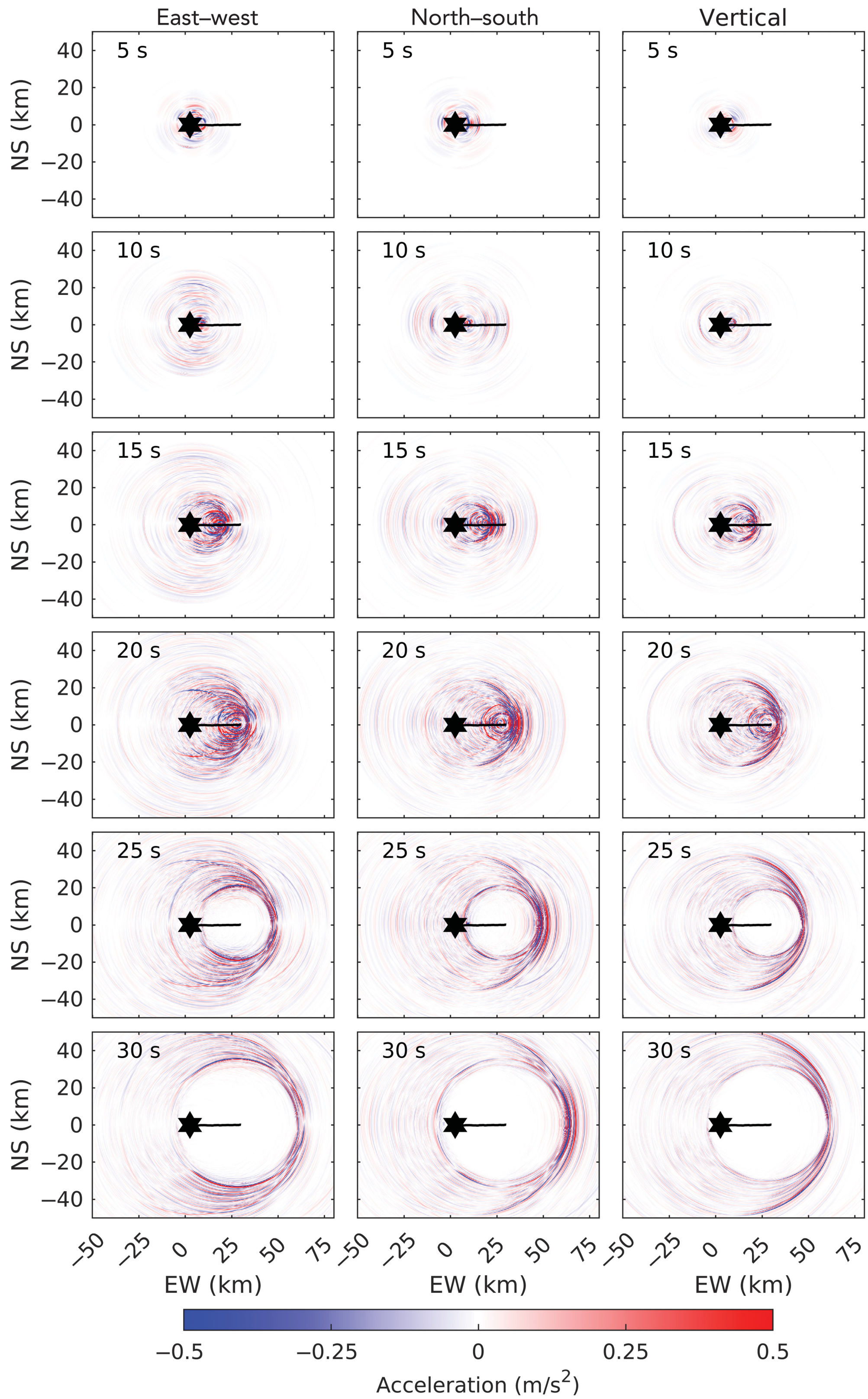

Figure 4. Snapshots of the east–west (EW), north–south (NS), and vertical components of ground acceleration at the Earth surface for model A1. The black star marks the epicenter, and the black line is the fault surface trace.

accurate up to frequencies of 6 Hz, essentially acting as a high-cut filter for our simulated waveforms. Because the PGA is influenced by a wide range of frequencies, including those above 6 Hz, the application of a high-cut filter to waveforms can affect PGA values (Douglas and Boore, 2011). Simulated PGAs can be higher if frequencies above 6 Hz are included, but the introduction of other physical processes, such as plastic deformation of rock material near the fault, intrinsic attenuation, and wavefield scattering at high frequencies, can lower PGAs. In addition, BEA14 is developed for tectonically active regions where strong motion data will have little energy from frequencies above 10 Hz due to high κ values (Douglas and Boore, 2011). Given these considerations, we approach the comparison of PGAs between our simulations and BEA14 with caution. Our primary goal in this comparative analysis is to assess the first-order accuracy and reliability of our simulations, focusing on two key aspects. First, we seek to determine whether the PGAs from our simulations exhibit a similar distance-decay pattern as observed in BEA14. Second, we aim to establish if the majority of the simulated PGAs fall within the two-sigma bounds of estimates from BEA14. The moment magnitude of simulated models varies in a narrow range, M_w 6.82–6.95 (see Table 2). Therefore, we use M_w 6.885 as a representative value to estimate PGAs from BEA14. Figure 6 reveals that most of the PGAs from simulations lie within two sigma bounds of BEA14. The box plot median of simulated PGAs is comparable to median estimates

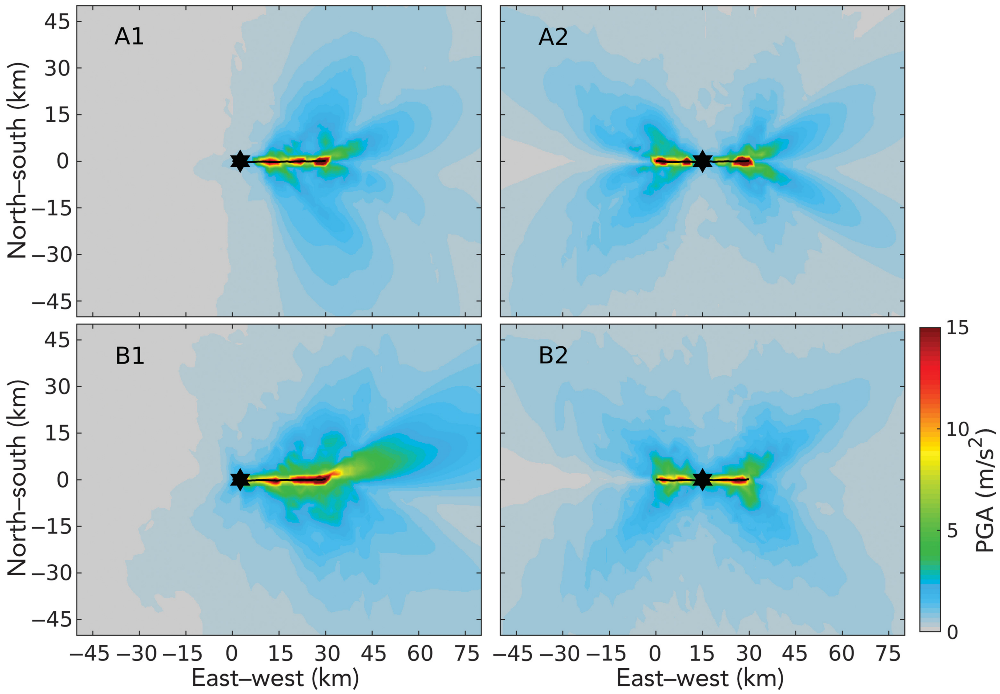

Figure 5. Spatial distribution of PGA at the Earth surface for four selected rough-fault models (A1, A2, B1, B2). The black star marks the epicenter, and the black line is a fault surface trace.

to qualitatively examine effects of rupture directivity on ground shaking and the resulting mismatch between simulated and empirically estimated PGAs. We observe that $PGA_{res} = 0$ represents identical PGA estimates from simulations and empirical GMM, and $PGA_{res} = 1$ and $PGA_{res} = -1$ mean simulated PGAs are ∼2.72 times larger and smaller, respectively, than estimates from BEA14.

Figure 7 depicts variations of PGA residuals for all 18 models at ten near-fault receivers (r1–r10, see Fig. 1). PGA_{res} is close to zero for all rupture models for receivers located in fault-normal (FN) direction (i.e., at receivers r5 and r6). PGA_{res} variations are large for stations in fault-parallel (FP) direction (i.e., at receivers r1 and r10) due to forward or backward rupture directivity effects. Similar effects on PGA_{res} can also be seen at receivers far from the fault (i.e., at receivers r11–r20, see Fig. S7). Furthermore, PGV residuals (PGV_{res}) also show similar patterns—nearly zero values in the FN direction and large variations in the FP direction (see Figs. S8 and S9). Empirical GMMs do not incorporate directivity effects in their statistical modeling for the median prediction. Therefore, larger variations in PGA_{res} and PGV_{res} are expected, especially for unilateral rupture models with pronounced rupture directivity. We thus examine PGA and PGV variations due to rupture directivity effects on ground-shaking variability from unilateral and bilateral ruptures in more detail.

from BEA14 at all distances. Moreover, 50% of simulated PGAs (boxes from box plots) are within one sigma bounds of BEA14. PGAs from simulations could be lower if we had included other natural physical processes such as plastic rock deformation of near-fault material or seismic wavefield scattering. Considering the dissipation of energy during plastic deformation may help reduce the large PGAs observed at some stations very close to the fault (Wollherr *et al.*, 2018). The absence of intrinsic attenuation and wavefield scattering due to small-scale heterogeneities can lead to higher simulated PGAs than estimated by BEA14, even at longer distances from the fault (Imperatori and Mai, 2013; Vyas *et al.*, 2018, 2021). However, the inclusion of these physical processes obscures the analysis of evaluating the effects of fault roughness on ground-shaking variability; therefore, we did not consider them. Overall, PGAs from simulations compare reasonably well with BEA14 (distance decaying trend and most within two sigma bounds), given the physical processes and modeling setup under consideration. Although the difference between box plot median and BEA14 median estimates grows with increasing R_{JB}, most of the simulated PGVs are within two sigma bounds of BEA14 (see Fig. S6).

Finally, we analyze the PGA residuals, defined as

$$PGA_{res} = \ln\left(\frac{PGA_{sim}}{PGA_{BEA14}}\right), \quad (3)$$

in which PGA_{sim} is the simulated PGA and PGA_{BEA14} is median estimate of PGA from BAE14. Equation (3) allows

ANALYSIS OF GROUND-MOTION VARIABILITY

In this section, we analyze ground-motion variability, that is, the variability of PGA and PGV as a function of distance, with respect to rupture propagation style (unilateral and bilateral ruptures) and fault roughness amplitude. We also compare average variability from all considered simulations to four empirical GMMs (BA08 [Boore and Atkinson, 2008], CB08 [Campbell and Bozorgnia, 2008], BEA14 [Boore *et al.*, 2014], and CB14 [Campbell and Bozorgnia, 2014]).

The virtual receiver network comprises a total of 3366 sites (Fig. 1). To compute the mean ($\mu_{\ln(PGA)}$ or $\mu_{\ln(PGV)}$) and standard deviation ($\phi_{\ln(PGA)}$ or $\phi_{\ln(PGV)}$) of ln(PGA) or ln(PGV), we bin receivers with respect to R_{JB} distance, using a bin width of 5 km. This approach yields 10 bins in a distance range from 1 to 51 km, with each bin containing at least 100 receivers.

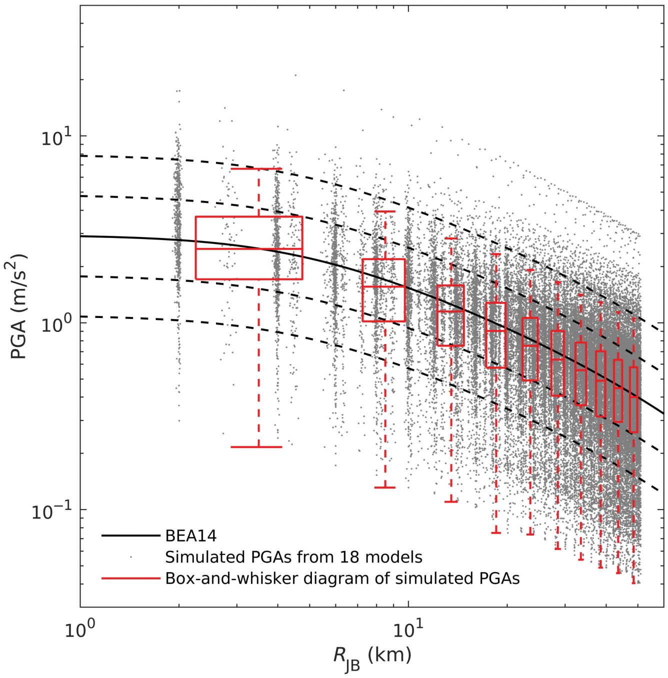

Figure 6. Comparison of PGA from rough-fault rupture simulations with estimates from the empirical ground-motion model (GMM; Boore *et al.*, 2014; BEA14). The solid and dashed lines (black color) represent the median and one-and-two sigma bounds, respectively, of PGA from BEA14. Simulated PGAs (gray dots) are combined into 10 R_{JB} distance bins (bin width 5 km) to generate box plots. In each box, the central mark is the median, and the bottom and top edges are representing the 25th and 75th percentiles, respectively, of PGAs in each bin; whiskers indicate 1.5 times the interquartile range.

Comparing within-event ground-motion variability ($\phi_{\ln(PGA)}$ or $\phi_{\ln(PGV)}$) to the four selected empirical GMMs allows to understand the effects of rupture directivity and fault roughness on variability and implications for seismic hazard assessment.

Effects of rupture style on ground-motion variability

To examine ground-motion variability for unilateral ruptures, we plot the distance dependence of $\mu_{\ln(PGA)}$ and $\phi_{\ln(PGA)}$ for the twelve unilateral rupture models in our database (Fig. 8; Table 2). The mean, $\mu_{\ln(PGA)}$, decreases with increasing R_{JB} distance from the fault (as expected from our aforementioned qualitative considerations). $\phi_{\ln(PGA)}$ remains nearly constant, and its amplitude varies compared to GMM-based estimates, suggesting the need to better understand the reasons for such variations. PGV variability ($\phi_{\ln(PGV)}$) is also nearly invariant with distance—a trend consistent with $\phi_{\ln(PGA)}$ (compare Fig. 8 and Fig. S10). For four rupture models (C1, D1i, D3i, and F3i), $\phi_{\ln(PGA)}$ is comparable to GMM estimates; however, for the remaining eight models (A1, B1, E1, F1, A3, B3, C3, and E3i), $\phi_{\ln(PGA)}$ is higher compared to those of GMMs. Especially, $\phi_{\ln(PGA)}$ for models A1, B1, A3, and E3i is almost twice as high compared to that of GMMs (~0.8–0.9 and ~0.5, respectively). We conjecture that this is due to very small PGA values in the backward directivity region (see Fig. S4). Consequently, in an R_{JB} bin, very large values in the forward directivity region are combined with very small values in the backward directivity region, leading to high $\phi_{\ln(PGA)}$ values.

For bilateral ruptures A2, B2, C2, D2, E2, and F2, the hypocenter is in the center of the fault, and hence directivity effects are reduced. Figure 9, depicting the distance dependence of $\mu_{\ln(PGA)}$ and $\phi_{\ln(PGA)}$ for six bilateral rupture models (Table 2), reveals that $\phi_{\ln(PGA)}$ decreases with increasing R_{JB} distance in the near field (≤20 km). Particularly, the $\phi_{\ln(PGA)}$ decreases nearly from 0.65 to 0.4 for model A2. At larger distances, the influence of small-scale rupture complexity on the radiated seismic wavefield is diminished, leading to almost constant PGA variability. For bilateral ruptures, the PGA variability is reduced (compared to unilateral ruptures) due to diminished directivity. $\phi_{\ln(PGA)}$ variations with R_{JB} distance show a more complicated pattern for bilateral ruptures compared to unilateral ruptures. In the near field, $\phi_{\ln(PGA)}$ for three models (A2, C2, and F2) is larger than empirical GMMs, whereas it is smaller for other models (B2, D2, and E2). However, $\phi_{\ln(PGA)}$ is comparable to or smaller than GMMs at larger distances (>20 km). The rupture complexity effects on ground shaking due to fault roughness are more pronounced in the near field, leading to larger $\phi_{\ln(PGA)}$ for some rupture models compared to GMMs at near-fault distances. PGV variability ($\phi_{\ln(PGV)}$) is smaller or comparable to empirical GMMs at all distances (Fig. S11), suggesting that PGA variations are more influenced in the near field than PGV variations due to rupture intricacies caused by fault roughness.

Effects of fault roughness amplitude on ground-motion variability

Next, we investigate how fault roughness influences ground-motion variability. Figure 10 summarizes the distance dependence of $\mu_{\ln(PGA)}$ and $\phi_{\ln(PGA)}$ for all the eighteen rupture models. For six pairs of models (A1–B1, A2–B2, A3–B3, C2–D2, C3–D3i, and E3i–F3i), we find that rougher faults produce ground motions with lower variability. However, for the two source-model pairs (C1–D1i and E1–F1), variability is comparable for both the levels of fault roughness. For one rupture-model pair (E2–F2), a rougher fault yields larger variability. Therefore, increased fault roughness is likely to produce lower ground-motion variability, because higher roughness causes stronger local acceleration or deceleration of the rupture front, leading to a spatially more distorted radiation pattern and hence a redistribution of wave amplitudes. Consequently, directivity effects may be diminished by large distortions in the radiated wavefield for some rough fault models, with higher roughness leading to lower ground-motion variability. For the majority of the rupture-model pairs, PGV variability is almost comparable for two roughness levels (see Fig. S12), suggesting less influence of fault roughness-driven rupture complexity on PGV levels than PGA variations.

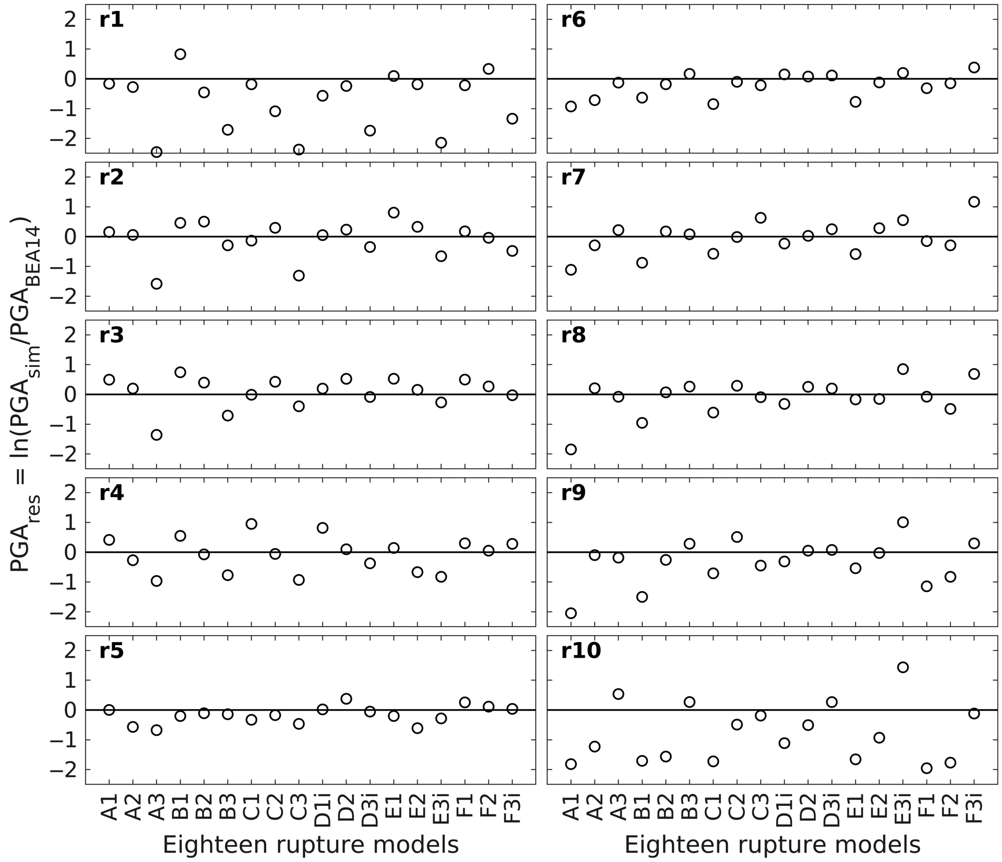

Figure 7. Residuals of simulated PGAs with respect to empirical GMM (Boore *et al.*, 2014; BAE14) at selected stations (r1–r10, see Fig. 1).

Average ground-motion variability from simulations

So far, we have focused on the results of individual simulations. To gain a more robust understanding, we now analyze the average variability by calculating the mean and standard deviation of $\phi_{\ln(\mathrm{PGA})}$ and $\phi_{\ln(\mathrm{PGV})}$, considering all the eighteen rupture models. The average PGA and PGV variabilities are almost constant (Fig. 11). Comparing the average PGA variability with GMM-based estimates reveals that although the GMM estimates lie within one standard deviation of the average variability, the simulation-based average PGA variability is higher by ≈0.1 log-normal units. However, the average PGV variability is comparable to estimates from empirical GMMs. Fault roughness causes acceleration and deceleration of rupture, radiating high frequencies that affect PGA more strongly than PGV. Therefore, we find that rupture intricacies caused by fault roughness have a larger impact on PGA variations (and hence variability) compared to PGV variability, resulting in higher average PGA variability (≈20%) compared to GMM estimates.

To further assess if average PGA variability is not biased by the larger number of unilateral compared to bilateral ruptures, we conduct the Jackknife test by randomly selecting six unilateral and (all) six bilateral rupture models from the entire set. Figure 12 depicts the distance dependence of the mean and standard deviation of $\phi_{\ln(\mathrm{PGA})}$ computed for nine different samples of twelve rupture models. We find that mean $\phi_{\ln(\mathrm{PGA})}$ is consistently larger than the empirical GMM estimates. Hence, on average, fault roughness yields higher ground-motion variability for PGA than empirically estimated. A similar Jackknife test for PGV variability shows that mean $\phi_{\ln(\mathrm{PGV})}$ is comparable to GMM estimates, suggesting that a large number of unilateral rupture models do not bias average PGV variability.

DISCUSSION AND CONCLUSIONS

In this study, we analyze the effects of fault roughness and rupture style based on hypocenter locations (causing unilateral or bilateral ruptures) on within-event ground-motion variability based on dynamic rupture simulations for which the seismically radiated wavefield reaches up ~6 Hz.

Our simulations indicate that ground-motion variability (considering both PGAs and PGVs) does not depend on R_{JB} distance for unilateral ruptures. This observation aligns with the trends reported by empirical GMMs. However, our findings are inconsistent with the results of the previous studies by Imtiaz *et al.* (2015) and Vyas *et al.* (2016), who reported a decline in ground-motion variability with increasing fault distance for unilateral ruptures in simulations. Both earlier investigations and our simulations emphasize considerable fluctuations in ground-motion variability for unilateral ruptures. For example, $\phi_{\ln(\mathrm{PGA})}$ and $\phi_{\ln(\mathrm{PGV})}$ from our simulations are in the range of 0.45–1.0 and 0.4–0.8, respectively, at $R_{\mathrm{JB}} = 10$ km. Similarly, studies by Imtiaz *et al.* (2015) and Vyas *et al.* (2016) suggest $\phi_{\ln(\mathrm{PGV})}$ in the range of 0.6–1.0 for equivalent distances. Regarding bilateral ruptures, our simulations demonstrate that $\phi_{\ln(\mathrm{PGA})}$ (or $\phi_{\ln(\mathrm{PGV})}$) decreases with increasing R_{JB} within the near-field region (up to 20 km). Beyond this range, the variability becomes almost constant. However, it is essential to observe that our variability analysis is limited to the R_{JB} distance range of 50 km. A prior study by Imtiaz *et al.* (2015) reported near-constant variability for

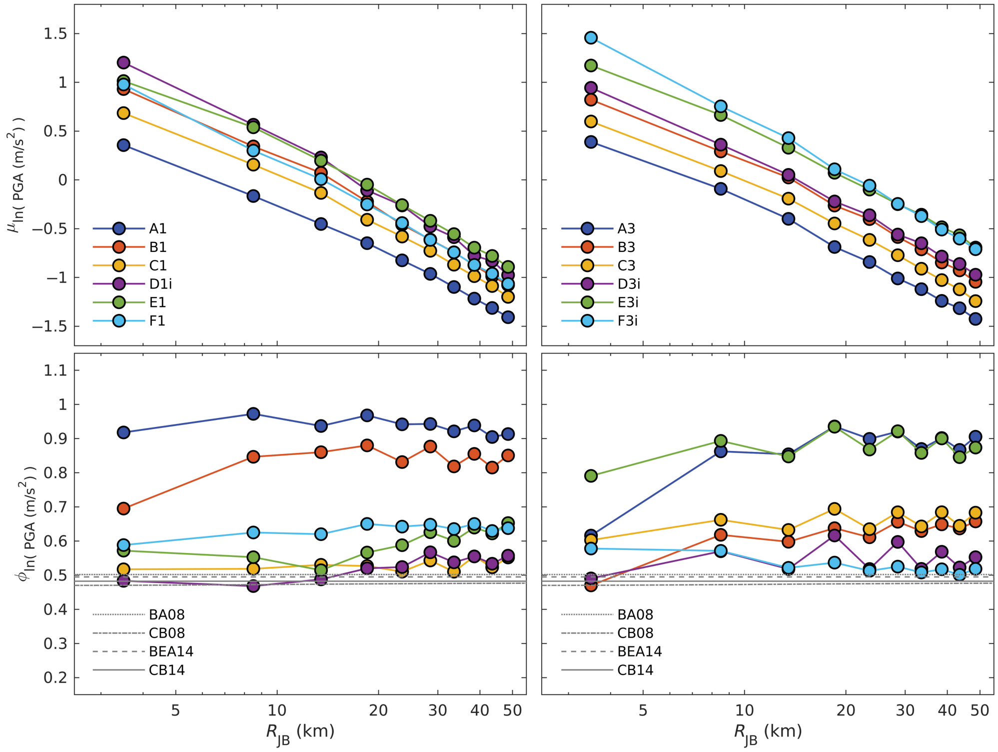

Figure 8. Distance dependence of the mean ($\mu_{\ln(PGA)}$) and the standard deviation ($\phi_{\ln(PGA)}$) of ln(PGA) for 12 unilateral dynamic rupture simulations. Indices 1 and 3 in model names indicate hypocenter location (see Fig. 2). For clarity, we use separate subplots for results for ruptures propagating toward the right and left (indices 1 and 3, respectively). Abbreviations are as follows: BA08, Boore and Atkinson (2008); CB08, Campbell and Bozorgnia (2008); BEA14, Boore *et al.* (2014); and CB14, Campbell and Bozorgnia (2014).

ground-motion variability can be partly attributed to variations in rupture propagation.

Ground-motion variability tends to be greater for unilateral ruptures compared to bilateral ruptures. A similar trend has been observed by Imtiaz *et al.* (2015), particularly within near-fault distances ($R_{JB} < 30$ km). Unilateral ruptures exhibit strong directivity effects, resulting in ground-motion amplification in the forward rupture direction (see Fig. 5). On the other hand, bilateral ruptures display more symmetrical ground-motion patterns with less pronounced directivity, leading to reduced variability. The directivity effect, arising from a combination of *S*-wave radiation pattern and rupture propagation direction, plays a crucial role in shaping the ground-motion characteristics of both the rupture types.

R_{JB} values below 50 km for bilateral ruptures. Thus, the ground-motion variability resulting from ruptures, both unilateral and bilateral, occurring on rough faults exhibits different trends compared to the findings of the previous simulation-based studies, which did not consider roughness variations.

Different modeling techniques, rupture properties, and resolved frequencies contribute to the differences observed in variability trends from our simulations and earlier studies for unilateral and bilateral ruptures. The previous studies by Imtiaz *et al.* (2015) and Vyas *et al.* (2016) used kinematic rupture models, and were limited to frequencies up to 3 Hz and 1 Hz, respectively, whereas our study includes high-frequency radiation up to ~6 Hz due to dynamic rupture on rough faults. Also, the on-fault slip variations in these dynamic simulations are smoother than those in two studies based on kinematic rupture models. Although our dynamic rupture modeling yields smooth slip distributions, simulated PGAs (and PGVs) are comparable to empirical estimates by BEA14 (see Fig. 6 and Fig. S6). Because the variations in rupture speed, due to acceleration and deceleration of the rupture fronts, are more pronounced in the dynamic rupture simulations than in the kinematic modeling by Imtiaz *et al.* (2015) and Vyas *et al.* (2016), the different behavior of

Fault roughness introduces distortion in the radiation pattern, and induces significant variations in rupture speed due to the acceleration and deceleration of the rupture front, further influencing rupture directivity. As a consequence, variations in rupture velocity can impact the directivity and ground-motion characteristics of both the types of ruptures, with a more prominent influence observed for unilateral ruptures.

Faults with higher amplitudes of roughness are likely to cause ground motions with lower variability of PGAs than faults with lower fault roughness (see Fig. 10). Fault roughness creates local barriers for rupture due to stress concentrations, resulting in the asymmetric radiation of seismic energy. Such a distorted radiation pattern will possibly lower rupture directivity, potentially lowering ground-motion variability. Fault roughness allows for the radiation of high-frequency seismic energy, which is expected to affect PGAs (and their variability) more than PGVs. Long-term earthquake simulations suggest that fault roughness can cause variable coseismic slip and hypocenters in restraining bends (i.e., locations with high stress) (e.g., Allam *et al.*, 2019). Such variations in slip distribution and hypocenter locations that create unilateral or bilateral ruptures are likely to affect rupture directivity. The recent study by Withers, Olsen, Day, *et al.*

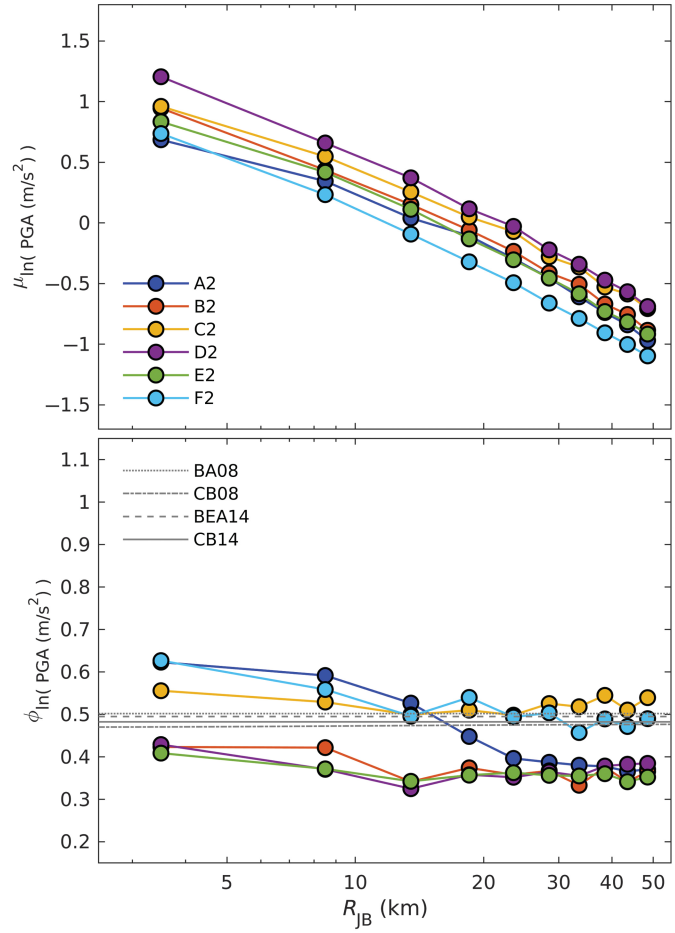

Figure 9. Distance dependence of the mean ($\mu_{\ln(\text{PGA})}$) and the standard deviation ($\phi_{\ln(\text{PGA})}$) of ln(PGA) for six bilateral ruptures (see Fig. 2). Abbreviations follow Figure 8.

(2019) suggests that small-scale random heterogeneities in Earth structure have a larger impact on ground-shaking variability than fault roughness. We do not consider such heterogeneities in Earth structure, because our main focus is to analyze the effects of fault roughness and rupture style on ground-shaking variability. However, the distance and frequency range over which seismic wavefield scattering due to medium heterogeneities becomes more important than the intricacies of the rupture process remain poorly understood and are a subject for future study.

Shi and Day (2013) conducted dynamic rupture simulations on a rough fault using rate-and-state friction with strong velocity weakening. They observed multiple seismic wave fronts that exhibited high-frequency radiation (~10 Hz) and distortion of the radiation pattern in acceleration snapshots (see their fig. 18). These observations are similar to the variations in acceleration wavefield snapshots that we observed in our study (Fig. 4) due to spontaneous rupture irregularities. In addition, the spatial variability pattern of PGAs obtained from their simulations resembles the PGA patterns from our bilateral ruptures (compare their fig. 21 with our Fig. 5). We did not consider off-fault inelastic deformation of material, in contrast to Shi and Day (2013), who introduced Drucker–Prager plasticity in their simulations. They observed that PGAs from simulations with plasticity are approximately 50% lower than those without plasticity. Although Shi and Day (2013) did not specifically focus on analyzing ground-motion variability, the ground-motion characteristics they reported, including multiple wave fronts and PGA patterns, are consistent with our study.

Graves and Pitarka (2016) conducted kinematic rupture simulations (~5 Hz) considering fault roughness, stochastic perturbations to velocity structure, and a damage zone surrounding the shallow fault surface. They investigated the relationship between fault roughness and the average Fourier amplitude spectrum (FAS) ratio of FN to FP components, observing that an increase in fault roughness leads to a decrease in the FN/FP FAS ratio for stations located in the forward directivity region (see their fig. 10). This reduction in the FN/FP FAS ratio implies a decrease in the coherence of radiated higher-frequency energy. In our study, we computed the FN/FP FAS ratios using waveforms from 20 stations (red circles in Fig. 1) and compared these ratios from three rupture models with lower roughness (A1, C1, and E1) against three models with higher roughness (B1, D1i, and F1), as illustrated in Figure 13. The median FN/FP FAS ratio resulting from higher roughness models is lower than that from lower roughness models for frequencies above 2 Hz, indicating reduced coherence of radiated energy and directional effects in ground motions. However, the median FN/FP FAS ratio in higher roughness models falls within the interquartile range of the lower roughness models, suggesting that they may not be statistically significant in models with higher roughness, although directivity effects and wavefield coherence are reduced. Overall, our findings are consistent with Graves and Pitarka (2016) in suggesting that fault roughness is associated with reduced coherence of radiated high frequencies.

The average variability from our eighteen simulated rupture models does not depend on distance, consistent with the distance-independent trend in the four empirical GMMs we used in this study. However, the average PGA variability is nearly 0.1 units (in log-normal scale, ≈20%) larger than the GMM estimates, whereas the average PGV variability is comparable to empirical estimates (Fig. 11). This higher ground-motion variability for PGAs affects seismic hazard curves (Bommer and Abrahamson, 2006). Moreover, the average $\phi_{\ln(\text{PGA})}$ from our simulations is nearly 0.6, whereas the past studies using kinematic rupture modeling suggest $\phi_{\ln(\text{PGA})}$ or $\phi_{\ln(\text{PGV})}$ between 0.5 and 1.0 (Imtiaz *et al.*, 2015; Vyas *et al.*, 2016; Gallovič, 2017; Crempien and Archuleta, 2018) at near-fault distances ($R_{JB} < 25$ km). Dynamic rupture modeling studies also suggest the standard deviation of spectral acceleration ($\phi_{\ln(\text{SA})}$) between 0.4 and 1.0 at these distances (Withers, Olsen, Day, *et al.*, 2019; Valentová *et al.*, 2021). Therefore, our average variability

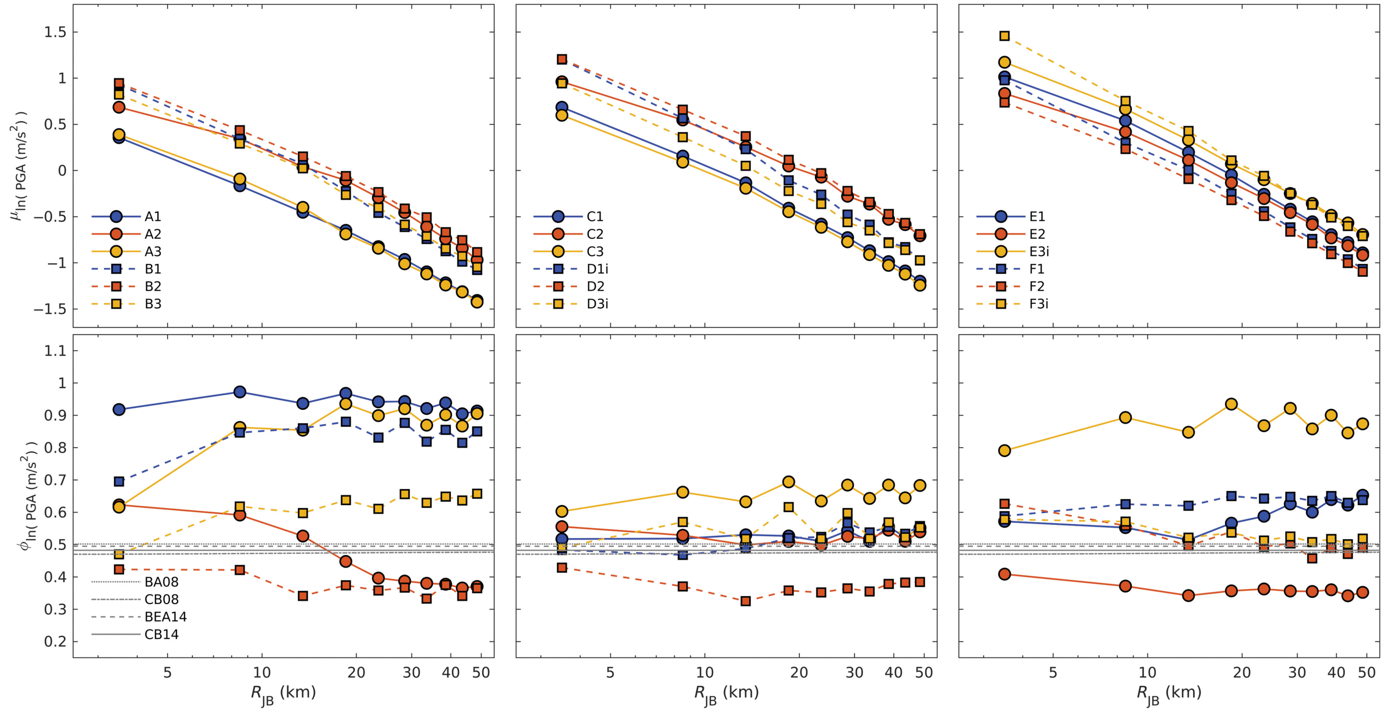

Figure 10. Effects of fault roughness on the mean ($\mu_{\ln(\mathrm{PGA})}$) and standard deviation ($\phi_{\ln(\mathrm{PGA})}$) of ln(PGA). The color indicates the realization of the spatial distribution of the fault roughness. The results for models with higher fault roughness are depicted by dashed lines, and the results for models with lower roughness are depicted by solid lines. Abbreviations follow Figure 8.

estimates are consistent with the previous kinematic and dynamic simulation studies, though broader variations of variability at near-fault distances require further investigation.

Although the PGAs obtained from simulations exhibit a favorable comparison with empirical GMM, they are not statistically equivalent. This discrepancy becomes evident, as only 50% of the simulated PGAs (as indicated by the boxes in the box plot) fall within the one-sigma bounds, as depicted in Figure 6. Furthermore, the average variability in PGAs derived from simulations exceeds estimates from empirical GMM, as highlighted in Figure 11. As a result, relying solely on ground-motion modeling based on fault roughness is insufficient to generate PGAs that maintain statistical consistency with empirical GMMs. Consequently, the future extensions of this research should encompass additional physical processes, such as inelastic deformation around the fault and seismic scattering due to small-scale heterogeneities, which has the potential to enhance agreement between simulation outcomes and empirical GMMs in statistical terms. Incorporating plastic deformation in dynamic rupture modeling has been shown to lead to peak-slip-rate saturation and a shift of the corner frequency toward lower frequencies when compared to assuming elastic rock behavior (Andrews, 2005; Shi and Day, 2013; Wollherr *et al.*, 2018). Moreover, the presence of heterogeneities in on-fault stress

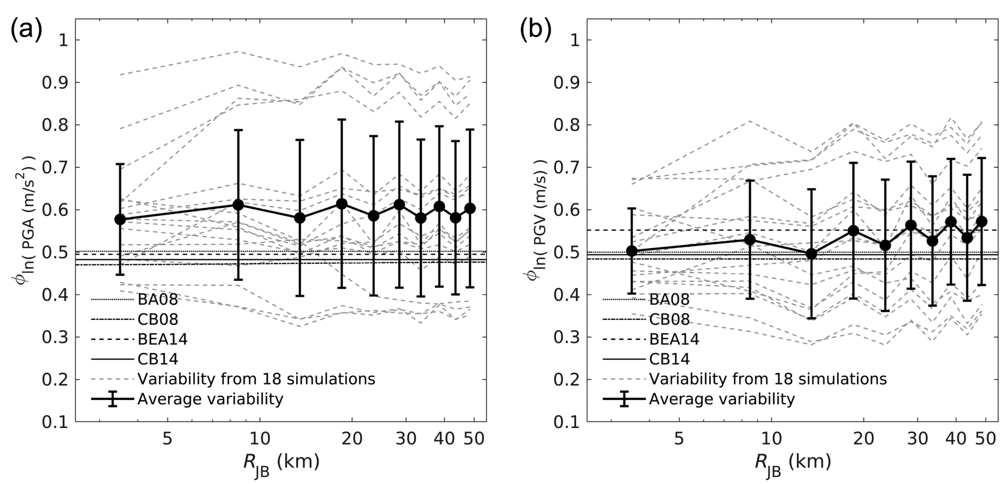

Figure 11. Distance dependence of the average (mean) of (a) $\phi_{\ln(\mathrm{PGA})}$ and (b) $\phi_{\ln(\mathrm{PGV})}$, and the associated standard deviation calculated for all eighteen considered rupture models (depicted by black thick solid lines and symbols). Variabilities ($\phi_{\ln(\mathrm{PGA})}$ or $\phi_{\ln(\mathrm{PGV})}$) of individual models are depicted by gray dashed lines. Abbreviations follow Figure 8.

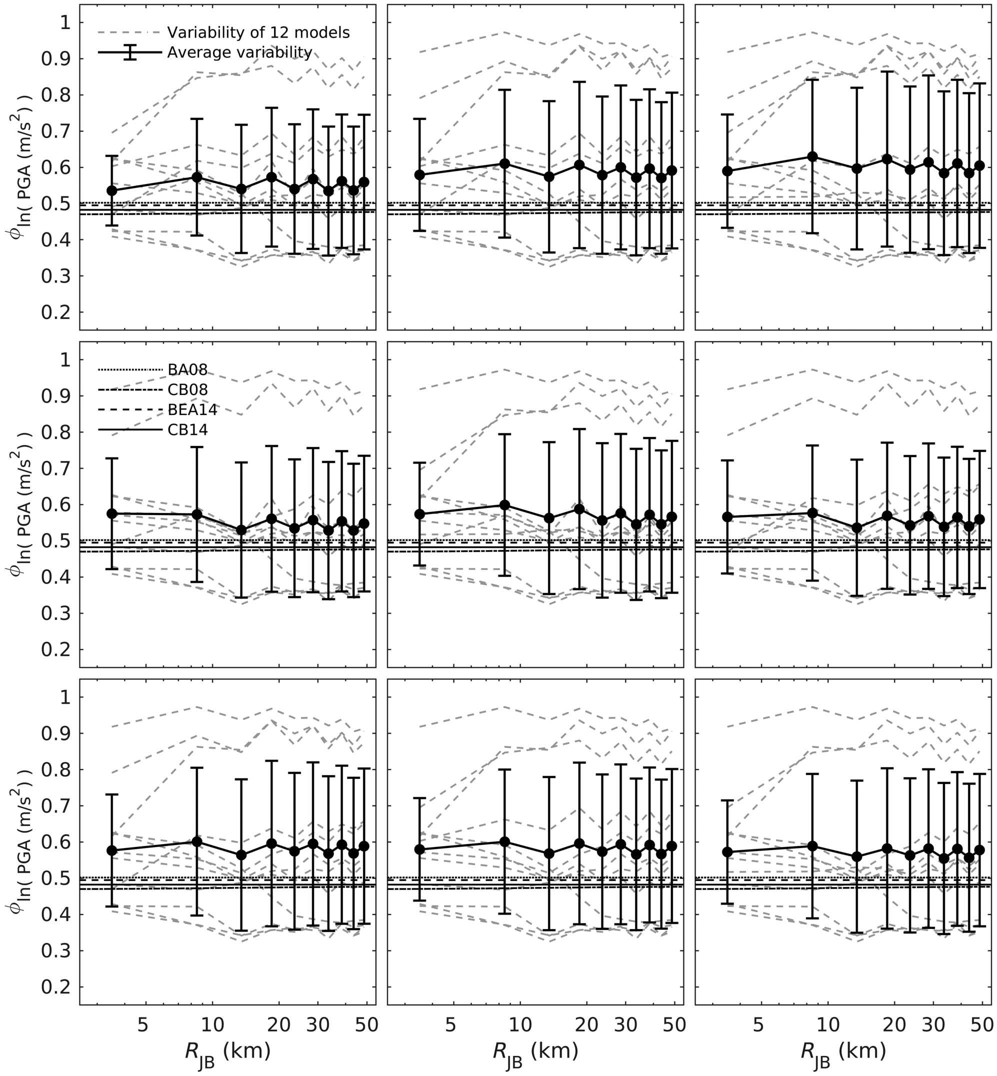

Figure 12. Jackknife test for the average (mean) of $\phi_{\ln(PGA)}$, considering nine different samples of sets of twelve rupture models combining six randomly selected unilateral and (all) six bilateral rupture models. Variabilities ($\phi_{\ln(PGA)}$) of individual models are depicted by gray dashed lines. Abbreviations follow Figure 8.

and frictional parameters causes stress drop variations on the fault, influencing earthquake slip, rupture speed, and the radiated high frequencies, which, in turn, affect ground-motion behavior and its variability (Brune, 1970, 1971; Ben-Zion, 2008; Ripperger *et al.*, 2008). In addition, small-scale heterogeneities in Earth's structure induce the scattering of high-frequency seismic waves, leading to the redistribution of seismic energy (Imperatori and Mai, 2013, 2015; Vyas *et al.*, 2018, 2021). This seismic scattering also distorts the seismic-wave radiation pattern, resulting in an apparent isotropic radiation pattern at high frequencies (Takemura *et al.*, 2009).

In summary, our dynamic rupture simulations help develop a physics-based understanding of how the amplitude of fault roughness and rupture styles affect earthquake ground-shaking variability at low and high frequencies using PGVs and PGAs, respectively. Our finding of average ground-shaking variability (for PGAs) from simulations being higher than empirical GMMs, especially by nearly 20%, has important implications for PSHA, especially for long return periods (Bommer and Abrahamson, 2006). Hence, findings in this study will inform the future research on assessing ground-motion variability from physics-based modeling and estimating seismic hazards for engineering applications.

DATA AND RESOURCES

In this study, we analyze ground-motion waveforms that result from dynamic rupture simulations by Mai *et al.* (2018). The maximum resolved frequency, $f_{max} \approx 5.75$ Hz for 40 s long seismic waveforms required nearly 2 hr on 128 × 64 Haswell cores of the Shaheen II supercomputer. We generated nearly 200 GB data by storing waveforms and wavefield snapshots. This article is accompanied by the supplemental material, which comprises rough-fault models, ground velocity waveforms, snapshots of ground velocity, peak ground acceleration (PGA) and velocity (PGV) maps, simulated PGVs comparison with empirical ground-motion models, PGA and PGV residuals, PGV variability as a function of unilateral ruptures, bilateral ruptures, and fault roughness variations.

DECLARATION OF COMPETING INTERESTS

No conflict of interests.

ACKNOWLEDGMENTS

This research is supported by King Abdullah University of Science and Technology (KAUST) in Thuwal, Saudi Arabia, under Grants BAS/1/1339-01-01 and URF/1/3389-01-01 (Jagdish Chandra Vyas and Paul Martin Mai). Earthquake rupture dynamics and ground-motion modeling have been carried out using the KAUST Supercomputing Laboratory (KSL), and the authors acknowledge the support of the KSL staff. Martin Galis acknowledges partial support from Slovak Foundation Grant VEGA 2/0046/20. The authors extend gratitude to Associate Editor Hiroshi Kawase, Reviewer Fabrice Cotton, and the anonymous reviewer for their constructive feedback to improve the content and presentation of our study.

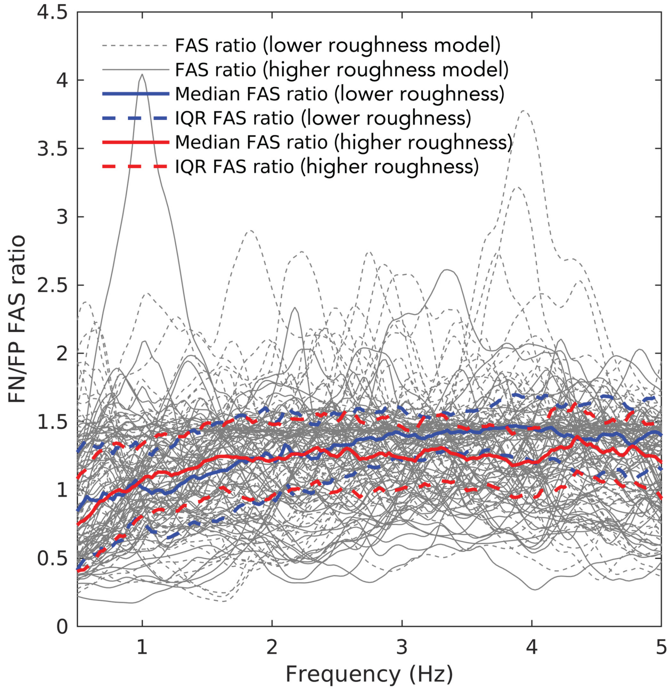

Figure 13. Comparing FAS ratios between FN and FP components at 20 stations (red circles in Fig. 1) for six rupture models. Dashed gray lines represent FN/FP FAS ratios for models with lower roughness (A1, C1, E1), whereas solid gray lines depict FN/FP FAS ratios for models with higher roughness (B1, D1i, F1). For models with lower roughness, median and interquartile range (IQR) values for FN/FP FAS ratios at these 20 stations are shown as solid and dashed blue lines, respectively. Similarly, for models with higher roughness, the median and IQR are illustrated by solid and dashed red lines, respectively.

REFERENCES

Abrahamson, N., and W. Silva (2008). Summary of the Abrahamson & Silva NGA ground-motion relations, *Earthq. Spectra* **24,** no. 1, 67–97.

Abrahamson, N. A., W. J. Silva, and R. Kamai (2014). Summary of the ASK14 ground motion relation for active crustal regions, *Earthq. Spectra*, **30,** no. 3, 1025–1055.

Allam, A., K. Kroll, C. Milliner, and K. Richards-Dinger (2019). Effects of fault roughness on coseismic slip and earthquake locations, *J. Geophys. Res.* **124,** no. 11, 11,336–11,349.

Anderson, J. G., and J. N. Brune (1999). Probabilistic seismic hazard analysis without the ergodic assumption, *Seismol. Res. Lett.* **70,** no. 1, 19–28.

Anderson, J. G., and S. E. Hough (1984). A model for the shape of the Fourier amplitude spectrum of acceleration at high frequencies, *Bull. Seismol. Soc. Am.* **74,** no. 5, 1969–1993.

Andrews, D. (2005). Rupture dynamics with energy loss outside the slip zone, *J. Geophys. Res.* **110,** no. B1, doi: 10.1029/2004JB003191.

Aochi, H., and J. Douglas (2006). Testing the validity of simulated strong ground motion from the dynamic rupture of a finite fault, by using empirical equations, *Bull. Earthq. Eng.* **4,** no. 3, 211–229.

Atik, L. A., N. Abrahamson, J. J. Bommer, F. Scherbaum, F. Cotton, and N. Kuehn (2010). The variability of ground-motion prediction models and its components, *Seismol. Res. Lett.* **81,** no. 5, 794–801.

Atkinson, G. (2013). Empirical evaluation of aleatory and epistemic uncertainty in eastern ground motions, *Seismol. Res. Lett.* **84,** no. 1, 130–138.

Atkinson, G. M., and D. M. Boore (2006). Earthquake ground-motion prediction equations for eastern North America, *Bull. Seismol. Soc. Am.* **96,** no. 6, 2181–2205.

Baumann, C., and L. A. Dalguer (2014). Evaluating the compatibility of dynamic rupture-based synthetic ground motion with empirical ground-motion prediction equation, *Bull. Seismol. Soc. Am.* **104,** no. 2, 634–652.

Beauval, C., L. Honoré, and F. Courboulex (2009). Ground-motion variability and implementation of a probabilistic–deterministic hazard method, *Bull. Seismol. Soc. Am.* **99,** no. 5, 2992–3002.

Ben-Zion, Y. (2008). Collective behavior of earthquakes and faults: Continuum-discrete transitions, progressive evolutionary changes, and different dynamic regimes, *Rev. Geophys.* **46,** no. 4, doi: 10.1029/2008RG000260.

Beresnev, I. A. (2019). Interpretation of kappa and fmax filters as source effect, *Bull. Seismol. Soc. Am.* **109,** no. 2, 822–826.

Bommer, J. J., and N. A. Abrahamson (2006). Why do modern probabilistic seismic-hazard analyses often lead to increased hazard estimates? *Bull. Seismol. Soc. Am.* **96,** no. 6, 1967–1977.

Boore, D. M., and G. M. Atkinson (2008). Ground-motion prediction equations for the average horizontal component of PGA, PGV, and 5%-damped PSA at spectral periods between 0.01 s and 10.0 s, *Earthq. Spectra* **24,** no. 1, 99–138.

Boore, D. M., W. B. Joyner, and T. E. Fumal (1997). Equations for estimating horizontal response spectra and peak acceleration from western North American earthquakes: A summary of recent work, *Seismol. Res. Lett.* **68,** no. 1, 128–153.

Boore, D. M., J. P. Stewart, E. Seyhan, and G. M. Atkinson (2014). NGA-West2 equations for predicting PGA, PGV, and 5% damped PSA for shallow crustal earthquakes, *Earthq. Spectra* **30,** no. 3, 1057–1085.

Boore, D. M., J. Watson-Lamprey, and N. A. Abrahamson (2006). Orientation-independent measures of ground motion, *Bull. Seismol. Soc. Am.* **96,** no. 4A, 1502–1511.

Brune, J. (1971). Correction [to "tectonic stress and the spectra, of seismic shear waves from earthquakes"], *J. Geophys. Res.* **76,** no. 20, 5002–5002.

Brune, J. N. (1970). Tectonic stress and the spectra of seismic shear waves from earthquakes, *J. Geophys. Res.* **75,** no. 26, 4997–5009.

Bydlon, S. A., K. B. Withers, and E. M. Dunham (2019). Combining dynamic rupture simulations with ground-motion data to characterize seismic hazard from M w 3 to 5.8 earthquakes in Oklahoma and Kansas, *Bull. Seismol. Soc. Am.* **109,** no. 2, 652–671.

Campbell, K. W., and Y. Bozorgnia (2008). NGA ground motion model for the geometric mean horizontal component of PGA, PGV, PGD and 5% damped linear elastic response spectra for periods ranging from 0.01 to 10 s, *Earthq. Spectra* **24,** no. 1, 139–171.

Campbell, K. W., and Y. Bozorgnia (2014). NGA-West2 ground motion model for the average horizontal components of PGA, PGV, and 5% damped linear acceleration response spectra, *Earthq. Spectra* **30,** no. 3, 1087–1115.

Chiou, B. S.-J., and R. R. Youngs (2006). Chiou and Youngs PEER-NGA empirical ground motion model for the average horizontal component of peak acceleration and pseudo-spectral acceleration for spectral periods of 0.01 to 10 seconds, *PEER Rept. Draft*, 219 pp.

Chiou, B. S.-J., and R. R. Youngs (2008). An NGA model for the average horizontal component of peak ground motion and response spectra, *Earthq. Spectra* **24,** no. 1, 173–215.

Chiou, B. S.-J., and R. R. Youngs (2014). Update of the Chiou and Youngs NGA model for the average horizontal component of peak ground motion and response spectra, *Earthq. Spectra* **30,** no. 3, 1117–1153.

Crempien, J. G., and R. J. Archuleta (2018). Within-event and between-events ground motion variability from earthquake rupture scenarios, in *Best Practices in Physics-based Fault Rupture Models for Seismic Hazard Assessment of Nuclear Installations*, Springer, Birkhäuser, Basel, 127–141, doi: 10.1007/978-3-0348-7875-3_5.

Douglas, J., and H. Aochi (2016). Assessing components of ground-motion variability from simulations for the Marmara Sea region (Turkey), *Bull. Seismol. Soc. Am.* **106,** no. 1, 300–306.

Douglas, J., and D. M. Boore (2011). High-frequency filtering of strong-motion records, *Bull. Earthq. Eng.* **9,** 395–409.

Dumbser, M., and M. Käser (2006). An arbitrary high-order discontinuous Galerkin method for elastic waves on unstructured meshes—II. The three-dimensional isotropic case, *Geophys. J. Int.* **167,** no. 1, 319–336.

Dunham, E. M., D. Belanger, L. Cong, and J. E. Kozdon (2011). Earthquake ruptures with strongly rate-weakening friction and off-fault plasticity, part 2: Nonplanar faults, *Bull. Seismol. Soc. Am.* **101,** no. 5, 2308–2322.

Ely, G. P., S. M. Day, and J.-B. Minster (2008). A support-operator method for viscoelastic wave modelling in 3-D heterogeneous media, *Geophys. J. Int.* **172,** no. 1, 331–344.

Ely, G. P., S. M. Day, and J.-B. Minster (2009). A support-operator method for 3-D rupture dynamics, *Geophys. J. Int.* **177,** no. 3, 1140–1150.

Frankel, A., E. Wirth, N. Marafi, J. Vidale, and W. Stephenson (2018). Broadband synthetic seismograms for magnitude 9 earthquakes on the Cascadia Megathrust based on 3D simulations and stochastic synthetics, part 1: Methodology and overall results, *Bull. Seismol. Soc. Am.* **108,** no. 5A, 2347–2369.

Galis, M., P. Moczo, and J. Kristek (2008). A 3-d hybrid finite-difference—finite-element viscoelastic modelling of seismic wave motion, *Geophys. J. Int.* **175,** no. 1, 153–184.

Galis, M., C. Pelties, J. Kristek, P. Moczo, J. Ampuero, and P. Mai (2015). On initiation of dynamic rupture propagation with linear slip-weakening friction, *Geophys. J. Int.* **200,** 888–907.

Gallovič, F. (2017). Azimuthal dependence of the ground motion variability from Scenario Modeling of the 2014 Mw6. 0 South Napa, California, earthquake using an advanced kinematic source model, *Pure Appl. Geophys.* **174,** no. 9, 3467–3478.

Graves, R., and A. Pitarka (2016). Kinematic ground-motion simulations on rough faults including effects of 3D stochastic velocity perturbations, *Bull. Seismol. Soc. Am.* **106,** no. 5, 2136–2153.

Graves, R. W., and A. Pitarka (2010). Broadband ground-motion simulation using a hybrid approach, *Bull. Seismol. Soc. Am.* **100,** no. 5A, 2095–2123.

Guatteri, M., P. M. Mai, G. C. Beroza, and J. Boatwright (2003). Strong ground-motion prediction from stochastic-dynamic source models, *Bull. Seismol. Soc. Am.* **93,** no. 1, 301–313.

Hanks, T. C. (1982). f max, *Bull. Seismol. Soc. Am.* **72,** no. 6A, 1867–1879.

Harris, R. A. (2004). Numerical simulations of large earthquakes: Dynamic rupture propagation on heterogeneous faults, in *Computational Earthquake Science Part II*, Donnellan, A., P. Mora, M. Matsu'ura, and X. Yin (Editors), Birkhäuser, Basel, 2171–2181 pp.

Harris, R. A., M. Barall, B. Aagaard, S. Ma, D. Roten, K. Olsen, B. Duan, D. Liu, B. Luo, K. Bai, *et al.* (2018). A suite of exercises for verifying dynamic earthquake rupture codes, *Seismol. Res. Lett.* **89,** no. 3, 1146–1162.

Hartzell, S., M. Guatteri, P. M. Mai, P.-C. Liu, and M. Fisk (2005). Calculation of broadband time histories of ground motion, Part II: Kinematic and dynamic modeling using theoretical Green's functions and comparison with the 1994 Northridge earthquake, *Bull. Seismol. Soc. Am.* **95,** no. 2, 614–645.

Imperatori, W., and P. M. Mai (2012). Sensitivity of broad-band ground-motion simulations to earthquake source and Earth structure variations: An application to the Messina Straits (Italy), *Geophys. J. Int.* **188,** no. 3, 1103–1116.

Imperatori, W., and P. M. Mai (2013). Broad-band near-field ground motion simulations in 3-dimensional scattering media, *Geophys. J. Int.* **192,** no. 2, 725–744.

Imperatori, W., and P. M. Mai (2015). The role of topography and lateral velocity heterogeneities on near-source scattering and ground-motion variability, *Geophys. J. Int.* **202,** no. 3, 2163–2181.

Imtiaz, A., M. Causse, E. Chaljub, and F. Cotton (2015). Is ground-motion variability distance dependent? Insight from finite-source rupture simulations, *Bull. Seismol. Soc. Am.* **105,** no. 2A, 950–962.

Iwaki, A., N. Morikawa, T. Maeda, and H. Fujiwara (2017). Spatial distribution of ground-motion variability in broadband ground-motion simulations, *Bull. Seismol. Soc. Am.* **107,** no. 6, 2963–2979.

Komatitsch, D., and J. Tromp (1999). Introduction to the spectral element method for three-dimensional seismic wave propagation, *Geophys. J. Int.* **139,** no. 3, 806–822.

Mai, P. M., M. Galis, K. K. Thingbaijam, J. C. Vyas, and E. M. Dunham (2018). Accounting for fault roughness in pseudo-dynamic ground-motion simulations, in *Best Practices in Physics-based Fault Rupture Models for Seismic Hazard Assessment of Nuclear Installations*, Springer Birkhäuser, Basel, 95–126, doi: 10.1007/978-3-319-72709-7_7.

Mai, P. M., W. Imperatori, and K. B. Olsen (2010). Hybrid broadband ground-motion simulations: Combining long-period deterministic synthetics with high-frequency multiple S-to-S backscattering, *Bull. Seismol. Soc. Am.* **100,** no. 5A, 2124–2142.

Mena, B., and P. M. Mai (2011). Selection and quantification of near-fault velocity pulses owing to source directivity, *Georisk* **5,** no. 1, 25–43.

Moczo, P., J. Kristek, M. Galis, P. Pazak, and M. Balazovjech (2007). The finite-difference and finite-element modeling of seismic wave propagation and earthquake motion, *Acta Phys. Slovaca* **57,** no. 2, 177–406.

Paolucci, R., I. Mazzieri, C. Smerzini, and M. Stupazzini (2014). Physics-based earthquake ground shaking scenarios in large urban areas, in *Perspectives on European Earthquake Engineering and Seismology*, A. Ansal (Editor), Springer, Cham, 331–359.

Papageorgiou, A. S., and K. Aki (1983a). A specific barrier model for the quantitative description of inhomogeneous faulting and the prediction of strong ground motion. Part I. Description of the model, *Bull. Seismol. Soc. Am.* **73,** no. 3, 693–722.

Papageorgiou, A. S., and K. Aki (1983b). A specific barrier model for the quantitative description of inhomogeneous faulting and the prediction of strong ground motion. Part II. Applications of the model, *Bull. Seismol. Soc. Am.* **73,** no. 4, 953–978.

Pardo-Iguzquiza, E., and M. Chica-Olmo (1993). The fourier integral method: An efficient spectral method for simulation of random fields, *Math. Geol.* **25,** no. 2, 177–217.

Ramirez-Guzman, L., R. W. Graves, K. B. Olsen, O. S. Boyd, C. Cramer, S. Hartzell, S. Ni, P. Somerville, R. A. Williams, and J. Zhong (2015). Ground-motion simulations of 1811–1812 New Madrid earthquakes, central United States, *Bull. Seismol. Soc. Am.* **105,** no. 4, 1961–1988.

Ripperger, J., P. Mai, and J.-P. Ampuero (2008). Variability of near-field ground motion from dynamic earthquake rupture simulations, *Bull. Seismol. Soc. Am.* **98,** no. 3, 1207–1228.

Shi, Z., and S. M. Day (2013). Rupture dynamics and ground motion from 3-D rough-fault simulations, *J. Geophys. Res.* **118,** no. 3, 1122–1141.

Spudich, P., and L. N. Frazer (1984). Use of ray theory to calculate high-frequency radiation from earthquake sources having spatially variable rupture velocity and stress drop, *Bull. Seismol. Soc. Am.* **74,** no. 6, 2061–2082.

Strasser, F. O., N. A. Abrahamson, and J. J. Bommer (2009). Sigma: Issues, insights, and challenges, *Seismol. Res. Lett.* **80,** no. 1, 40–56.

Sun, X., B. Clayton, S. Hartzell, and S. Rezaeian (2018). Estimation of ground-motion variability in the central and eastern United States using deterministic physics-based synthetics, *Bull. Seismol. Soc. Am.* **108,** no. 6, 3368–3383.

Takemura, S., T. Furumura, and T. Saito (2009). Distortion of the apparent S-wave radiation pattern in the high-frequency wavefield: Tottori-Ken Seibu, Japan, earthquake of 2000, *Geophys. J. Int.* **178,** no. 2, 950–961.

Taufiqurrahman, T., A.-A. Gabriel, T. Ulrich, L. Valentova, and F. Gallovič (2022). Broadband dynamic rupture modeling with fractal fault roughness, frictional heterogeneity, viscoelasticity and topography: The 2016 mw 6.2 Amatrice, Italy earthquake, *Geophys. Res. Lett.* **49,** no. 22, e2022GL098872, doi: 10.1029/2022GL098872.

Valentová, L., F. Gallovič, and S. Hok (2021). Near-source ground motions and their variability derived from dynamic rupture simulations constrained by NGA-West2 GMPEs, *Bull. Seismol. Soc. Am.* **111,** no. 5, 2559–2573.

Vyas, J. C., M. Galis, and P. M. Mai (2021). Characterizing seismic scattering in 3D heterogeneous earth by a single parameter, *Bull. Seismol. Soc. Am.* **111,** no. 2, 791–800.

Vyas, J. C., P. M. Mai, and M. Galis (2016). Distance and azimuthal dependence of ground-motion variability for unilateral strike-slip ruptures, *Bull. Seismol. Soc. Am.* **106,** no. 4, 1584–1599.

Vyas, J. C., P. M. Mai, M. Galis, E. M. Dunham, and W. Imperatori (2018). Mach wave properties in the presence of source and medium heterogeneity, *Geophys. J. Int.* **214,** no. 3, 2035–2052.

Withers, K. B., K. B. Olsen, S. M. Day, and Z. Shi (2019). Ground motion and intraevent variability from 3D deterministic broadband (0–7.5 Hz) simulations along a nonplanar strike-slip, *Bull. Seismol. Soc. Am.* **109,** no. 1, 229–250.

Withers, K. B., K. B. Olsen, Z. Shi, and S. M. Day (2019). Validation of deterministic broadband ground motion and variability from dynamic rupture simulations of buried thrust earthquakes, *Bull. Seismol. Soc. Am.* **109,** no. 1, 212–228.

Wollherr, S., A.-A. Gabriel, and C. Uphoff (2018). Off-fault plasticity in three-dimensional dynamic rupture simulations using a modal discontinuous Galerkin method on unstructured meshes: Implementation, verification and application, *Geophys. J. Int.* **214,** no. 3, 1556–1584.

Manuscript received 28 May 2023
Published online 14 December 2023